Selection of doublet cellular patterns in directional solidification through spatially periodic perturbations

W. Losert, D. A. Stillman, and H. Z. Cummins

Department of Physics, City College of the City University of New York, New York, New York 10031

P. Kopczyński, W.-J. Rappel, and A. Karma

*Department of Physics and Center for Interdisciplinary Research on Complex Systems, Northeastern University,
Boston, Massachusetts 02115*

Pattern formation at the solid-liquid interface of a growing crystal was studied in directional solidification using a perturbation technique. We analyzed both experimentally and numerically the stability range and dynamical selection of cellular arrays of ''doublets'' with asymmetric tip shapes, separated by alternate deep and shallow grooves. Applying an initial periodic perturbation of arbitrary wavelength to the unstable planar interface allowed us to force the interface to evolve into doublet states that would not otherwise be dynamically accessible from a planar interface. We determined systematically the ranges of wavelength corresponding to stable singlets, stable doublets, and transient unstable patterns. Experimentally, this was accomplished by applying a brief UV light pulse of a desired spatial periodicity to the planar interface during the planar-cellular transient using the model alloy Succinonitrile-Coumarin 152. Numerical simulations of the nonlinear evolution of the interface were performed starting from a small sinusoidal perturbation of the steady-state planar interface. These simulations were carried out using a computationally efficient phase-field symmetric model of directional solidification with recently reformulated asymptotics and vanishing kinetics [A. Karma and W.-J. Rappel, Phys. Rev. E **53** R3017 (1996); Phys. Rev. Lett. **77**, 4050 (1996); Phys. Rev. E **57**, 4323 (1998)], which allowed us to simulate spatially extended arrays that can be meaningfully compared to experiments. Simulations and experiments show remarkable qualitative agreement in the dynamic evolution, steady-state structure, and instability mechanisms of doublet cellular arrays. [S1063-651X(98)02310-1]

PACS number(s): 68.70.+w

I. INTRODUCTION

Material properties of solidified alloys depend on the macroscopic shape of the sample and the alloy composition, but they are also strongly influenced by microscopic patterns (microstructure), often in the form of local variations in the concentration of alloy components. Pattern formation is typically studied in directional solidification where a sample is pulled through a linear temperature gradient at a constant velocity V_P. After an initial transient, the crystal reaches a constant growth velocity and, in most cases, the solid-liquid interface settles into a steady-state pattern. This process gives rise to a rich variety of interfacial patterns that have been of fundamental and technological interest for several decades (see [2] for a review). At low pulling velocity the interface is stabilized by the temperature gradient and remains simply planar. Above a critical velocity V_C the planar interface undergoes the classic Mullins-Sekerka instability [3]. This morphological instability occurs because the destabilizing effect of the diffusion field overcomes the stabilizing effects of the thermal gradient and surface tension over an intermediate range of wavelengths. It typically leads in a nonlinear regime to a spatially periodic array of small-amplitude cells for V_P close to V_C. In an intermediate range of velocities where V_P is a few times V_C, the grooves become deeper and narrower. Finally, in the high-velocity regime where V_P is much larger than V_C, the cells develop sidebranches and the array pattern becomes dendritic.

In recent years, it has become clear that the range of possible steady-state patterns that form in directional solidification is richer than one would have anticipated. Jamgotchian, Trivedi, and Billia (JTB) [4] observed the spontaneous formation of doublet cells for a small range of velocities between those producing small amplitude cells and deep cells. This symmetry-broken doublet pattern is characterized by alternating deep and shallow grooves and asymmetric cell shapes with the cell tip closer to the shallow groove. Hence the basic, spatially repeating, subunit of these structures consists of two asymmetric cells that are mirror images of each other about the growth axis, in contrast to conventional singlet states that consist of identical symmetrical cells with grooves of equal depth. JTB also occasionally observed the formation of isolated triplets (i.e., groups of three cells with a symmetrical cell sandwiched between two asymmetrical cells), but doublets were by far more preponderant.

Following these observations, Kopczyński *et al.* [5] carried out a boundary integral calculation of steady-state cellular structures in the symmetric model of directional solidification. These calculations revealed the existence of branches of doublets and higher-order multiplets (triplets, quadruplets, etc.) with narrow grooves. Shallower doublet cells had also been found previously by the same method [6] close to the onset of instability. Kopczyński *et al.* found that branches of multiplets bifurcate off the large spacing side of the main singlet branch. Furthermore, these bifurcation points were shown to be related to the stability properties of the singlet branch [5,7]. The calculated shapes of both dou-

blets and triplets were found to be in good qualitative agreement with the states observed by JTB.

Dendritic doublets have been observed experimentally in directional solidification by Akamatsu et al. [8], albeit in a higher velocity range than the one corresponding to cellular doublets. Although both types of doublet structures have the same symmetry, they may have a different branch origin. Dendritic doublets are most likely related to the doublon dendrite branch pinpointed by Ihle and Müller-Krumbhaar in simulations of unconstrained growth in a pure undercooled melt [9]. These solutions should be applicable to the tip region of directionally solidified dendrites that can be considered to be isothermal. In contrast, as shown by Kopczyński et al. [5], cellular doublets are only one branch of a whole series of multiplet branches that bifurcate off the main branch of singlet and are only observed for lower velocities.

At present, several very basic pattern stability and selection questions regarding cellular multiplets remain unanswered. Numerical calculations [10] and experiment [11] have so far given only a consistent picture of the stability of the singlet branch. While the boundary integral calculations of Kopczyński et al. [5] indicated the existence of a range of steady-state patterns for doublets, they did not determine their stability or show under which conditions doublets can evolve from an unstable planar interface. There is only a qualitative explanation for the upper and lower stability limits of doublets proposed by JTB. On the low-velocity side, small-amplitude cells tend to have flat tips that are prone to tip splitting, a mechanism that JTB found experimentally as limiting the region of stability. On the high-velocity side the grooves become deeper so the relative difference in groove depth becomes smaller, which makes the cell tips more symmetric. It is not known, however, whether these processes are precisely the ones that limit the range of stable doublets. Moreover, it is not known how stability limits may depend on crystalline anisotropy, which has been shown both theoretically [5] and experimentally [8] to play a crucial role in the singlet branch stability. In particular, it is now understood that without anisotropy, there are no stable cellular arrays of singlets, except in an extremely narrow range of velocity near V_C [5]. Is the same true for doublets?

With regard to selection, the results of numerical calculations [5] have left open the possibility that qualitatively different patterns (singlets, doublets, and higher-order multiplets) could be simultaneously stable under the same solidification conditions. Moreover, JTB measured doublet stability by determining which patterns are selected spontaneously as a function of pulling velocity, but could not explore other patterns that could be selected from different initial conditions.

The main goal of this paper is to explore these stability and selection issues by a combination of experiment and phase-field model simulations in the velocity regime close to that in which doublets were observed by JTB. The range of stable doublet patterns and the nature of the limiting instabilities are determined by forcing the interface into stable (or transiently unstable) patterns for a range of spacings. Experimentally, this is accomplished by applying a brief pulse of a spatially periodic perturbation to the planar interface during the planar-cellular transient. (A similar procedure was used previously by Curtis and Maher [12] in the context of viscous fingering.) Numerically, this process is simulated by applying a small sinusoidal perturbation of corresponding wavelength to the unstable steady-state planar interface and studying its evolution. One additional advantage of simulation, which substantially complements the experiment, is that we can vary at will the ratio of the system size to the wavelength. This allows us to pinpoint more accurately the instability mechanism of doublets. Moreover, we can explore stability properties as a function of crystalline anisotropy.

We find that stable doublets can be triggered for a range of spatial periodicities and growth velocities and that in this range both doublets and single cells can be created as stable patterns under the same steady-state growth conditions. Which structure is selected depends on which initial condition is used, i.e., a planar interface with a small amount of noise (corresponding to thermal fluctuations in the experiment and a small initial random perturbation of the planar interface in the simulation) or a deterministically modulated interface. For perturbation wavelengths or growth velocities outside the range in which stable doublet patterns are obtained, the forced doublet patterns are dynamically unstable and decay. Furthermore, we find that two distinct oscillatory instabilities with a wavelength equal to twice the cell spacing limit the range of stability of doublets and that there are no stable doublets for zero anisotropy. Overall, phase-field model simulations and experiments show remarkable qualitative agreement in the dynamic evolution, steady-state structure and in the mechanisms limiting doublet stability for small or large spacings. The agreement indicates that the common features of the experiments and the simulations must play an important role in determining pattern stability and selection.

II. EXPERIMENTS

A. Experimental procedure

The major component of the dilute binary alloy model system used in our experiments is the transparent organic crystal Succinonitrile (SCN) (Fluka Chemical Co.) which is widely used in directional solidification studies [4,13–15]. As solute the laser dye Coumarin 152 (C152, Sigma Chemical Co.) is added in small concentrations. C152 is used because it absorbs light in the near UV, which allows thermal perturbation of the sample through absorption of UV light and also makes a direct determination of the concentration possible through fluorescence measurements. All material parameters necessary for a quantitative comparison to theoretical predictions have been measured for the SCN-C152 system (see Table I). The SCN-C152 alloy is best described by the one-sided model of directional solidification [16]. The liquidus slope m and the segregation coefficient k are independent of solute (C152) concentration in the small concentration limit. Diffusion of C152 in the solid is orders of magnitude slower than in the liquid and can be neglected. Similarly, thermal diffusion of latent heat can be neglected since it is orders of magnitude faster than solute diffusion and therefore has negligible influence on the temperature gradient in the directional solidification experiment.

The SCN is four times vacuum distilled and then mixed under vacuum with C152 and filled into precleaned $0.1 \times 2 \times 150$ mm^3 glass capillaries (Vitro Dynamics). The capillar-

TABLE I. Selected material parameters of the model Succinonitrile-Coumarin 152 alloy.

Parameter		Ref.
segregation coefficient k	0.05	[17]
liquidus slope m	5.43 K/mol %	[17]
diffusion constant D	450 μm^2/s	[17]
interfacial free energy γ (SCN)	8.95 10^{-15} J/μm^2	[18]
melting temperature T_M (SCN)	331.2 K	[18]
latent heat (SCN)	4.627 10^{-11} J/μm^3	[18]
thermal conductivity (solid SCN)	5.36 10^{-4} cal/cms	[18]
surface tension anisotropy ϵ_4	0.55%	[19]
molecular weight (SCN)	80.09 g/mol	[18]
molecular weight (C152)	257 g/mol	[20]

ies are then flame sealed while keeping the sample under vacuum at all times. This procedure is necessary to ensure a long sample lifetime (>1 yr) since the SCN-C152 mixture quickly degrades under contact with air or epoxy [21].

The sample is inserted into an oil filled temperature gradient setup described in [22]. A single crystal, oriented in the (100) direction without grain boundaries is grown in the sample through a procedure described in detail in [17]. To move the sample through the temperature gradient the capillary is attached to a high-precision translation stage driven by a computer controlled dc motor. The temperature gradient G, measured with a thermocouple inserted into one sample, is linear and independent of the pulling velocity of the sample. This directional solidification setup is mounted onto a Nikon inverted microscope equipped with a charge coupled device (CCD) camera.

The microscope is also equipped with a 100 W mercury fluorescence lamp (100W/2 Osram) and UV optics. One mercury emission line at $\lambda = 404$ nm lies within the broad absorption peak of C152 ($\lambda_{max} = 394$ nm). Illuminating the sample with the mercury lamp leads to absorption by C152, which heats the sample. Even though the temperature increase is small, it leads to visible melting when the UV light is focused onto the solid-liquid interface (a temperature change of 10 mK changes the interface position by 5 μm for $G = 20$ K/cm). A reference sample without C152 shows no sign of heating under UV illumination.

A metal mask with seven rows of uniformly spaced holes (with different spacing for each row) is put into the shutter slot of the UV lamp and projected onto the sample. When one row of UV spots is positioned along the solid-liquid interface it causes localized melting of the solid. This spatially periodic melting produces an approximately sinusoidal modulation along the interface with a well defined wavelength λ_P. The perturbation wavelengths currently obtainable in our apparatus with this method range from 150 μm (limited by machinability of the mask and low total UV intensity per spot) up to 1000 μm (limited by the sample size).

The image of the solid-liquid interface, captured either directly from the CCD camera or from a videotape, is analyzed on a Macintosh IIci computer with digital image analysis software. The interface shape is extracted with a resolution of up to 0.3 μm, approximately one-tenth of one pixel [23]. (Parallel to the temperature gradient along the z axis 1 pixel$=3.17$ μm; perpendicular to the temperature gradient along the x axis 1 pixel$=3.29$ μm.) Since in our experiment the visible interface pattern comprises fewer than 20 wavelengths it is Fourier transformed through direct calculation of the Fourier integral for more than 100 wave vectors. The Fourier integral technique provides the amplitude and wavelength of the biggest Fourier component with high accuracy.

Before each experiment the oriented single crystal sample is held at rest in the directional solidification apparatus for 20–100 h to allow equilibration of the concentration profile. Equilibration is very slow since the solute spike that builds up and moves ahead of a planar or cellular interface in the experiments [17] displaces the solute over macroscopic distances (>1 cm). All experiments are carried out by starting the video camera recorder and elapsed time counter and switching on the pulling motor after 60 s. The motor reaches the selected pulling velocity V_P in 2 ms. The shutter for UV illumination is opened during the experiment at specified times for 1 min with the row of UV spots aligned along the solid-liquid interface. Since UV illumination causes a perturbation of the thermal field, it is applied for 1 min to allow the concentration field to adjust to the modulated interface shape. After 1 min the characteristic diffusion length ΔZ_1 is approximately equal to the perturbation wavelength and the characteristic length of the concentration spike ΔZ_2. ($\Delta Z_1 = \sqrt{4Dt} = 329$ μm, $\Delta Z_2 = D/V_P = 450$ μm at $V_P = 1$ μm/s). Due to fast thermal diffusion the relaxation of the temperature profile modulation is neglected in the analysis and only a modulated concentration profile is assumed.

The perturbation method was developed to measure the growth and decay rates of spatially periodic modulations of the interface pattern for a large range of wavelengths, which allows a detailed experimental "stability analysis" of the interface to be carried out. It was successfully applied in the analysis of the initial instability of a planar interface [17] and to analyze the stability of a dendritic array. In addition to measurements of a given pattern, however, the perturbation can also influence the evolution toward the steady-state interface pattern and can lead to new stable steady-state patterns. This aspect of the perturbation method was exploited in the present experiments.

Figure 1 shows, from bottom to top, a typical evolution of the interface pattern for a sample with solute concentration $C = 0.30$ wt. % and a temperature gradient $G = 16$ K/cm, when the motor is started after 1 min with a pulling velocity $V_P = 1.0$ μm/s ($V_P = 13.4V_C$, where V_C is the pulling velocity corresponding to the Mullins-Sekerka onset). The times indicated on this figure are taken from the elapsed time counter, so that 1:00 corresponds to the time when the pulling motor is switched on. Initially the interface is planar and shows no sign of an instability (9:30 min) since it takes time for the destabilizing solute concentration spike to build up ahead of the interface. At 10:00 min the UV illumination shutter is opened for 1 min and a perturbation with $\lambda_P = 256$ μm is applied to the solid-liquid interface. The UV intensity adds to the regular illumination intensity and is visible as a row of white spots (10:30 min). The modulated interface shape persists after the perturbation is switched off (11:30 min). Subsequently, the interface curvature in the grooves gradually gets larger, while it gets smaller in the cell tip region (28:00 min). Eventually the tip region of each cell splits into three cells (32:00 min). The middle cell of each
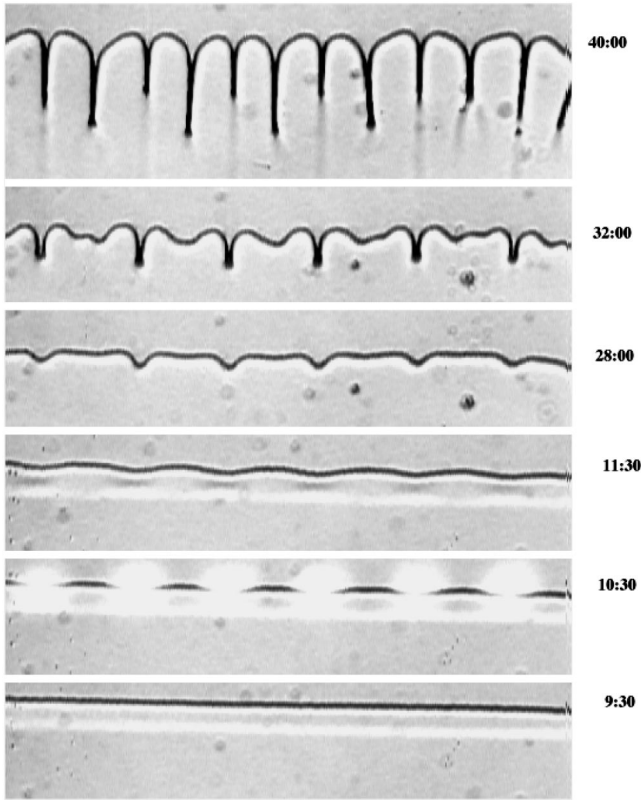
FIG. 1. Image sequence of the evolution of a forced doublet structure [SCN-C152, $C = 0.30$ wt. %, $\lambda_P = 256$ μm, $V_P = 1.0$ μm/s ($V_P = 13.4V_C$), and $G = 16$ K/cm]. From bottom to top: 9:30 min planar transient; 10:30 min UV perturbation; 11:30, 28:00, and 32:00 min doublet evolution; 40:00 min steady-state forced doublets.

triplet has a smaller amplitude and is overgrown by its neighboring cells. The groove between the two remaining cells becomes deeper than the grooves from the original modulation leading to an asymmetric doublet cellular structure in steady state (40:00 min). The final steady-state spacing of the doublets is determined by the wavelength of the applied perturbation.

B. Experimental results

Using the perturbation technique described above to obtain doublets, we first compare this forced doublet evolution to unperturbed experiments, then determine the parameter region where doublets are stable, and finally analyze the limiting instabilities. A comparison between a perturbed and an unperturbed experiment, both under the same growth conditions [$C = 0.30$ wt. %, $V_P = 1.0$ μm/s ($V_P = 10.6V_C$), and $G = 20.2$K/cm], shows the dynamics of forced doublet formation in detail. In experiment 1 the motor is started at $t = 0$ s (when the elapsed time counter reads 60 s) and 1 min perturbations are applied at $t = 240$ s and $t = 840$ s with $\lambda_P = 286$ μm ($k_P = 0.022$ μm^{-1}).

Figure 2 shows (from bottom to top) the interface profile extracted with our image analysis program every 120 s starting at $t = 720$ s during the evolution from a sinusoidal modulation and following the steady-state doublet cellular array. Figure 3 shows the Fourier transform of the interface for wave vectors between 0.01 and 0.1 μm^{-1} extracted every 60
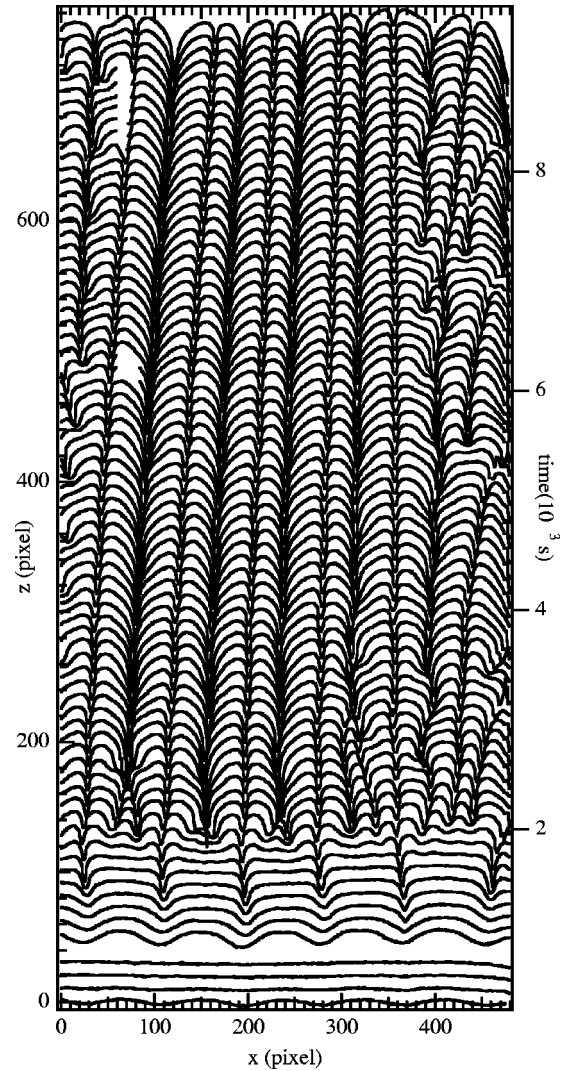

FIG. 2. Extracted interface shape for SCN-C152 [$C = 0.30$ wt. %, $\lambda_P = 286$ μm, $V_P = 1.0$ μm/s ($V_P = 10.6V_C$), and $G = 20.2$ K/cm]. Evolution to doublets from bottom to top: perturbation at 240 s decays, perturbation at 840 s evolves into doublets. Initial grooves become shallow grooves of doublets. (x axis, 1 pixel=3.29 μm; z axis, 1 pixel=3.17 μm.)

s starting at $t = 960$ s highlighting the evolution of the doublet structure until a steady state is reached. As seen in Fig. 2, the perturbation applied at $t = 240$ s leads to an approximately sinusoidal modulation of the planar interface with $\lambda_P = 286$ μm. The amplitude of the interface modulation decays exponentially after the perturbation is switched off, indicating that the planar interface is still stable. The reason is that the destabilizing concentration spike ahead of the solid-liquid interface takes time to build up so that the planar interface remains stable against perturbations for some time after crystal growth is started, as calculated by Warren and Langer [24] and measured by Losert, Shi, and Cummins [17].

The perturbation applied at $t = 840$ s again modulates the planar interface profile with $\lambda_P = 286$ μm. The amplitude of the modulation initially decreases again, but now goes through a minimum and starts to grow. This indicates that the interface is stable against perturbations of wavelength $\lambda_P = 286$ μm at $t = 840$ s when the perturbation is applied,
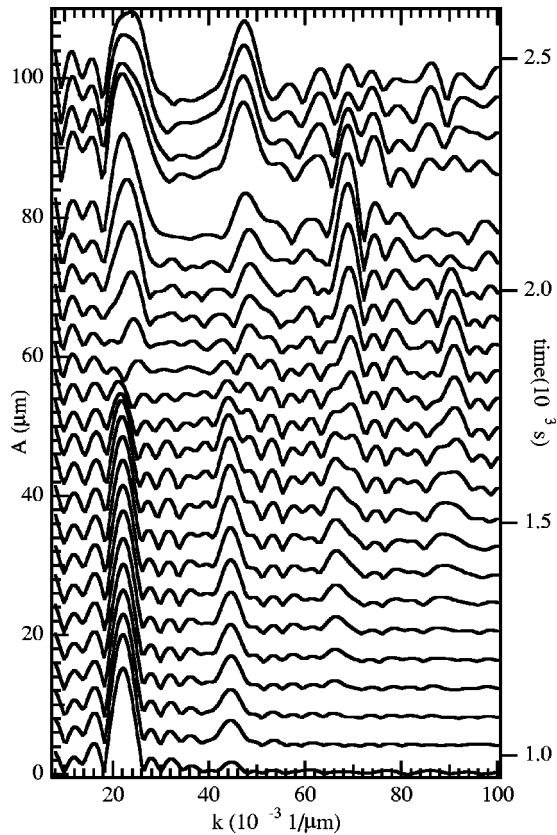
FIG. 3. Fourier transform of the interface profiles during doublet formation [same experiment as in Fig. 2: $C = 0.30$ wt. %, $\lambda_P = 286$ μm ($k_P = 0.022$ μm^{-1}), $V_P = 1.0$ μm/s ($V_P = 10.6V_C$), and $G = 20.2$ K/cm]. Doublets evolve through growth of second, third, and fourth harmonics of the applied perturbation wavelength.

but becomes unstable before the modulation amplitude has decayed completely. During the decrease of the modulation amplitude with wavelength $\lambda_P = 286$ μm the interface changes its shape as the region between grooves flattens ($t \approx 900$ s until $t = 1500$ s in Fig. 2). As a result the Fourier amplitudes of the harmonics of $\lambda_P = 286$ μm grow visibly ($t = 900$ s until $t = 1500$ s in Fig. 3). Eventually the flat region between grooves becomes unstable at $\lambda_P/3 = 95.3$ μm in most regions ($t = 1800$ s in Fig. 2) as the amplitude of the third harmonic starts to increase rapidly, reducing the other Fourier components, especially $\lambda_P = 286$ μm (Fig. 3). The middle cell of each triplet falls back quickly during coarsening and a doublet pattern is established after ~ 3000 s. The initial modulation wavelength determines the doublet spacings and the grooves of the initial modulation evolve into the small grooves of the steady-state doublets. This asymmetric doublet pattern exhibits two characteristic peaks in the Fourier transform and remains stable for the entire experimental run of more than 5 h. Since the width of the sample is not much larger than the extracted interface portion, perturbations caused by the finite sample width can become visible on either side of the analyzed interface section. In this case the influence of the sample wall is visible in Fig. 2 for $x > 400$ pixels. Slight misalignment of the crystalline axis causes a slow sideways drift ($< 1°$) of the stable doublet structure without destroying the basic pattern.

The evolution of the unperturbed interface is observed in experiment 2 under conditions otherwise identical to experi-
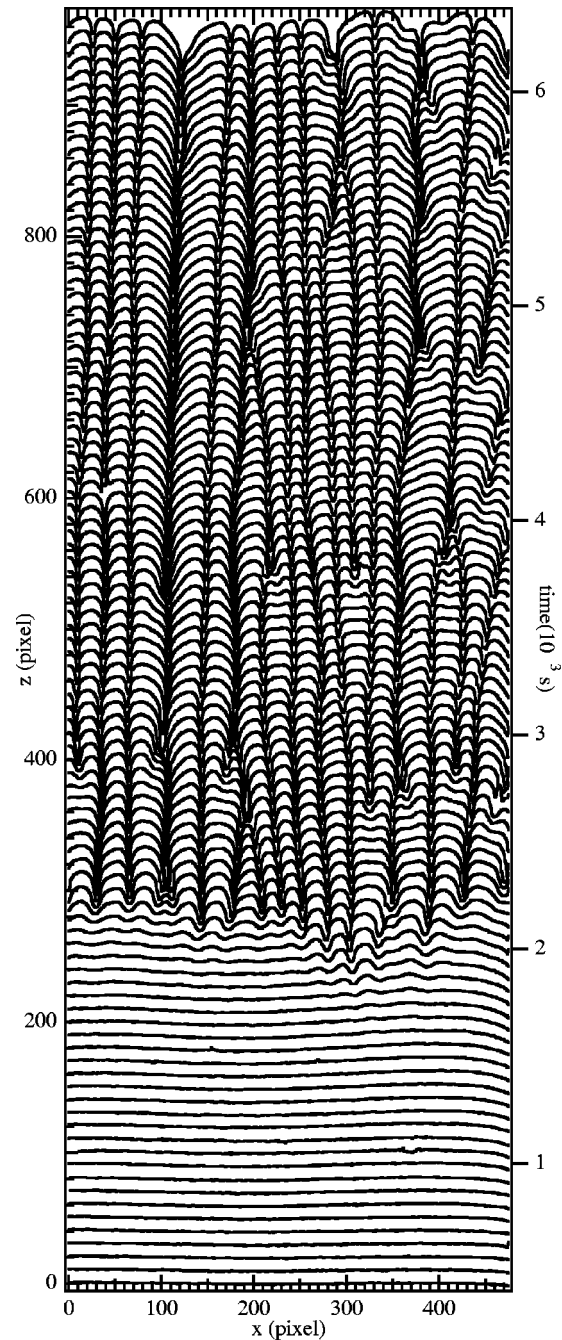

FIG. 4. Extracted interface structure for SCN-C152 [$C = 0.30$ wt. %, $V_P = 1.0$ μm/s ($V_P = 10.6V_C$), and $G = 20.2$ K/cm]. Unperturbed ''standard'' experiment. Interface extracted every 120 s starting at $t = 720$ s (x axis, 1 pixel$= 3.29$ μm; z axis: 1 pixel $= 3.17$ μm.)

ment 1. The interface shape, extracted every 120 s starting at $t = 720$ s is shown in Fig. 4.

At $t = 840$ s (when the UV perturbation was applied in experiment 1) the unperturbed interface is still planar. At $t \approx 2000$ s an initial spontaneous instability becomes visible with $\lambda_U \approx 91$ μm, approximately 1/3 of $\lambda_P = 286$ μm in experiment 1. The evolution in experiment 1 from λ_P to $\lambda_P/3$ thus involves the harmonic of the applied perturbation wavelength closest to the ''natural'' initial instability wavelength $\lambda_U \approx 91$ μm, in agreement with other experiments [17].

TABLE II. Observed interface pattern for unperturbed interfaces with three different perturbation wavelengths at two temperature gradients. ($C=0.30$ wt. % and $V_P=0.8$ μm/s).

Perturbation	$G=20$ K/cm	$G=16$ K/cm
unperturbed	some spontaneous doublets	chaotic pattern
$\lambda_P=246$ μm	doublets	weak doublets
$\lambda_P=282$ μm	doublets	doublets
$\lambda_P=318$ μm	slowly decaying doublets	chaotic pattern

In this unperturbed experiment the cellular pattern does not settle down but continuously evolves through tip splitting and cell overgrowth eventually showing signs of a rather inhomogeneous and slowly developing doublet structure at $t=6000$ s. The evolution is slower than observed by JTB, possibly because no grain boundaries (which can initiate doublet formation) are present in any of the samples we used.

These experiments show that stable forced doublets (experiment 1) of a selected wavelength can be created under growth conditions for which there is a ''weak'' tendency to create doublets spontaneously (experiment 2). While spontaneous doublets may occur gradually in unperturbed experiments after some time, they can be induced directly through a spatially periodic perturbation of suitable wavelength (which sets the doublet spacing), applied before the planar interface goes unstable. Fourier analysis of the pattern shows significant amplitudes only for harmonics of the perturbation wavelength during the formation of the doublet pattern.

To estimate the parameter region where forced doublets are stable we carried out a series of four experiments, each at two temperature gradients, all with $C=0.30$ wt. % at $V_P=0.8$ μm/s. In three experiments different perturbation wavelengths ($\lambda_P=246$ μm, $\lambda_P=282$ μm, and $\lambda_P=318$ μm) were applied and one experiment was carried out without perturbation.

At $G=20$ K/cm ($V_P=8.6V_C$) in the unperturbed experiment, parts of the interface slowly evolve into doublets, which shows a weak tendency towards a stable doublet state. For $\lambda_P=246$ and 282 μm stable doublets develop, while for $\lambda_P=318$ μm the interface shows doublets only initially that decay after $t\approx9000$ s evolving into an unstable pattern with no indication of settling down.

The unperturbed experiment at $G=16$ K/cm ($V_P=10.7V_C$, a lower G is equivalent to higher velocity) shows no settling down of the pattern (chaotic pattern) resembling the pattern evolution found by JTB for a velocity above the range where doublets are observed (see Fig. 12 in [4]). With $G=16$ K/cm only the perturbation with $\lambda_P=282$ μm produces a strong doublet state; the perturbation with $\lambda_P=246$ μm produces a weak doublet state showing almost single cells and for $\lambda_P=318$ μm no settling down of the pattern is observed. The range of stable doublet spacings thus appears larger for growth parameters where some doublets are observed in an unperturbed experiment. Outside that parameter region creation of doublets is still possible, but is limited to a small range of stable doublet spacings. The results are summarized in Table II.

The mechanisms limiting the range of stable doublet spacings are illustrated in Figs. 5 and 6, which are taken from a set of experiments with $C=0.20$ wt. %, $G=15.8$ K/cm, and $V_P=1.0$ μm/s. The mechanism limiting doublet pattern stability in the large-perturbation wavelength limit is shown in Fig. 5. After a perturbation with $\lambda_P=308$ μm is applied at $t=1200$ s the interface initially evolves into a doublet pattern. This pattern exhibits a ''breathing'' instability from the start, which is visible as an oscillation of the deeper (darker) grooves. Eventually one of the oscillations leads to the birth of a new cell at $t=10\,000$ s creating a triplet.

Figure 6 shows the evolution of the pattern in the small-perturbation wavelength limit, when a perturbation with $\lambda_P=236$ μm is applied at $t=1200$ s. Initially a doublet state with comparatively small asymmetry develops, but at $t\approx6000$ s an oscillatory instability becomes observable, which leads to broadening of every other cell and eventually to the falling back of one of the cells. The pattern does not appear to stabilize, even after 12 000 s. While the oscillatory motion is limited to deep grooves in the large-perturbation wavelength limit, the positions of all grooves oscillate in the small-perturbation wavelength limit. As will emerge from the phase-field calculations presented in Sec. III, the oscillatory motion for small doublet spacing is related to the oscillatory instability that has been calculated [10] and observed experimentally [11] to limit the stability of singlet cells for large spacing.

When the perturbation wavelength is even smaller, stable single cells can be obtained. Figure 7 [taken from another set of experiments with $C=0.22$ wt. %, $V_P=1.0$ μm/s ($V_P=13.9V_C$), and $G=11.3$ K/cm] shows two experiments under the same growth conditions but with different perturbation wavelengths [in Fig. 7(a) $\lambda_P=246$ μm; in Fig. 7(b) $\lambda_P=318$ μm] applied at $t=1800$ s before the planar interface becomes unstable.

Figure 7(a) shows the evolution of the interface towards steady-state single cells when a small-wavelength perturbation ($\lambda_P=246$ μm) is applied. The tips of the initial cellular modulation become unstable at $\lambda_P/2$ (45:00 min). A transient doublet structure is observed (60:00 min). The doublets decay into a steady-state single cell structure (120:00 min) with uniform wavelength. [This evolution is qualitatively very similar to results of numerical simulations carried out close to V_C (Fig. 3 of [25]).] Figure 7(b) shows the evolution of the interface towards steady-state doublets when a large-wavelength perturbation ($\lambda_P=318$ μm) is applied. Now the doublet structure that is again observed at 60:00 min remains stable in the steady state (120:00 min). This experiment thus shows that both singlet and doublet patterns can be stable under identical growth conditions, as suggested by the boundary integral calculations.

The dynamical evolution of doublets and the instability mechanisms found experimentally (as discussed in this sec-
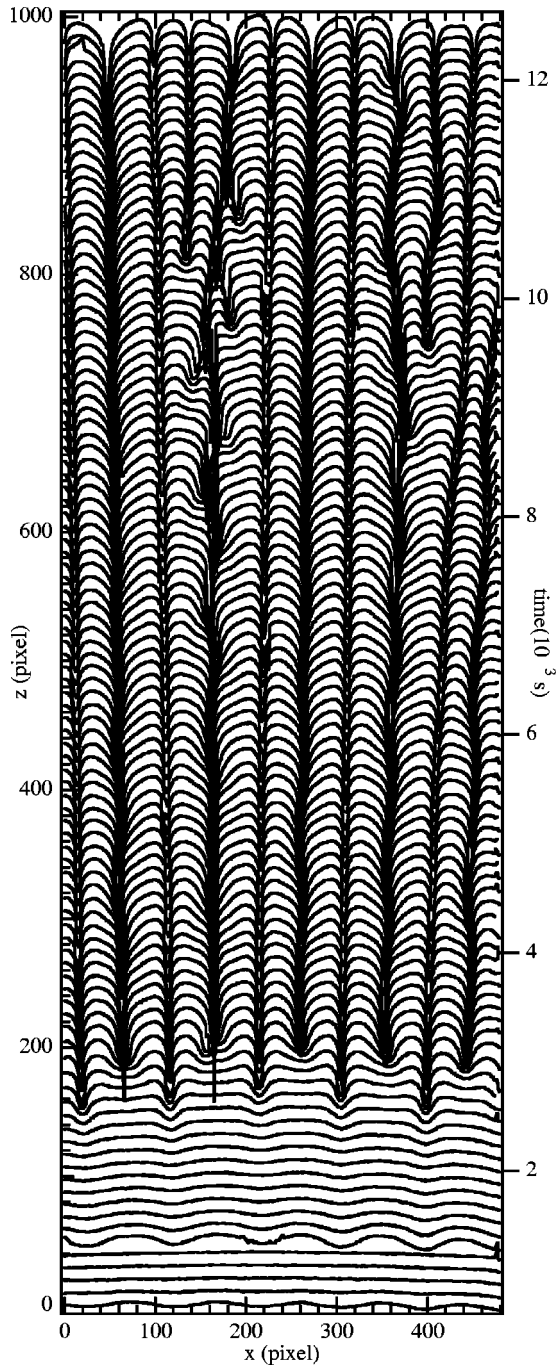
FIG. 5. Breathing instability of a doublet structure in the large-perturbation wavelength limit for SCN-C152 [$C = 0.22$ wt. %, $\lambda_P = 308$ μm, $V_P = 1.0$ μm/s ($V_P = 9.9V_C$), and $G = 15.8$ K/cm]. Interface extracted every 120 s starting from $t = 720$ s. (x axis, 1 pixel=3.29 μm; z axis, 1 pixel=3.17 μm.)

FIG. 6. Oscillatory instability of a doublet structure in the small-perturbation wavelength limit for SCN-C152 [$C = 0.22$ wt. %, $\lambda_P = 236$ μm, $V_P = 1.0$ μm/s ($V_P = 9.9V_C$), and $G = 15.8$ K/cm]. Interface extracted every 120 s starting from $t = 720$ s. (x axis, 1 pixel=3.29 μm; z axis, 1 pixel=3.17 μm.)

tion) are in good qualitative agreement with computer simulations using an improved phase-field model (which will be discussed in detail in the following section). Conclusions from both the experiments and the simulations will be discussed and compared in Sec. IV.

III. COMPUTATIONS

A. Phase-field model

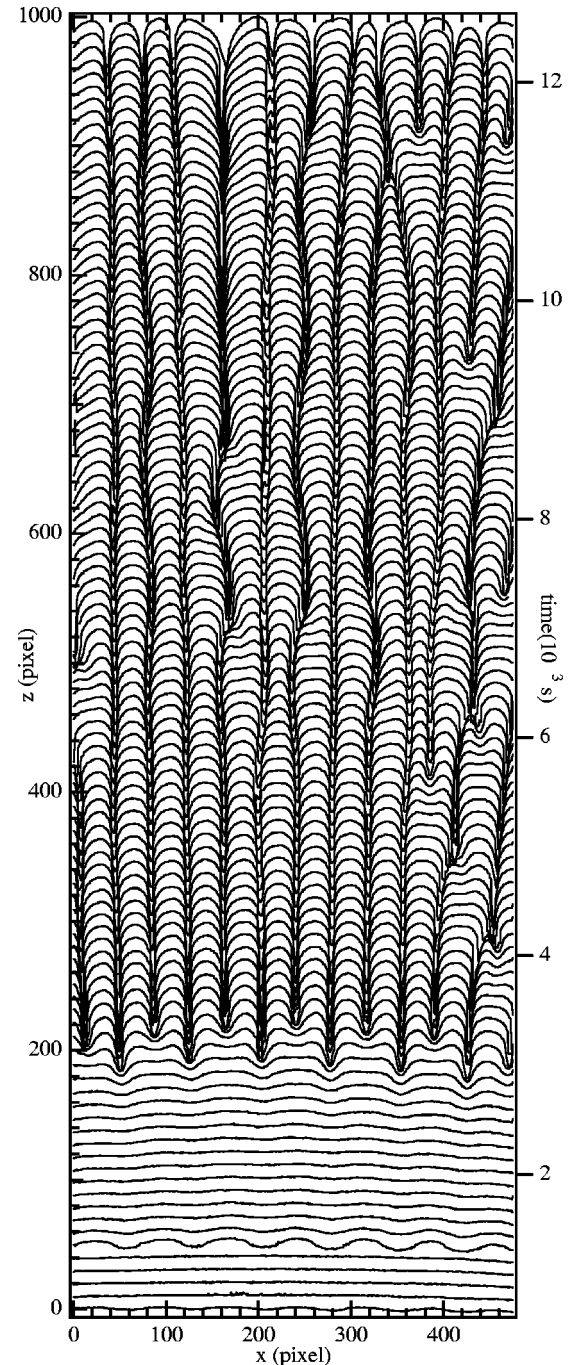The phase-field approach [26] has emerged as a powerful method to solve the class of free-boundary problems that

govern interfacial pattern formation phenomena during solidification. As is well known, this method avoids the usual difficulties of front tracking by introducing a "phase field," denoted here by ψ, to distinguish between the solid and liquid phases. As a result, it also introduces back into the problem a spatially diffuse interface region of thickness $\sim W$, where the phase field varies rapidly between two constant values, which is absent in the standard sharp-interface formulation of the free-boundary problem. The price to pay for reintroducing this interface region is that W typically needs
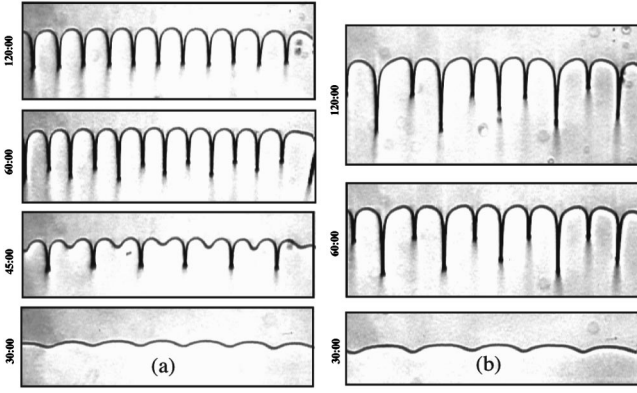
FIG. 7. Image sequence of the evolution to steady-state patterns [SCN-C152: $C = 0.22$ wt. %, $V_P = 1.0$ μm/s ($V_P = 13.9 V_C$), and $G = 11.3$ K/cm]. (a) Small-wavelength perturbation $\lambda_P = 246$ μm: transient doublets and steady-state single cells. (b) Large-wavelength perturbation $\lambda_P = 318$ μm: steady-state doublets.

to be chosen quite small compared to the scale of the solidification pattern (typical radius of curvature of the interface), which leads to extremely long computation time on large lattices. Recently, Karma and Rappel have shown that, for the solidification of a pure melt, this stringent computational constraint can be greatly diminished by reformulating the asymptotic analysis of the phase-field equations in the limit of a thin interface [1]. This analysis makes it possible to perform considerably more efficient computations with a smaller ratio d_0/W of capillary length to interface thickness. Moreover, it allows one to choose computational parameters so as to obtain a Gibbs-Thomson condition for the temperature field with an arbitrary kinetic coefficient. This is especially useful to simulate the regime of vanishing kinetics that is experimentally relevant for low velocity. The method has already been successfully applied to perform quantitative computations of dendritic growth in both two and three dimensions [1,27].

In this paper we exploit the fact that the asymptotics of Karma and Rappel [1] for a pure melt extends straightforwardly [28] to a phase-field model of directional solidification where (i) the concentration jump ΔC at the interface is constant (i.e., the liquidus and solidus lines are parallel in the phase diagram) and (ii) the solute diffusivities in the solid and liquid phases are equal. The sharp-interface limit of this model is precisely the symmetric model introduced originally by Langer and Turski [29,30]. One limitation of this model is that it cannot be used for a direct quantitative comparison with the present experiments, which are better described quantitatively by the standard one-sided model with nonequal solidus and liquidus slopes and zero diffusivity in the solid. Moreover, the simulations were performed with the solute concentration field assumed to be in steady state, while in the experiments the instability always occurs while the concentration field is evolving with time [17]. Consequently, the experiments are somewhat sensitive to the time at which the perturbation is applied, while the simulations are more sensitive to the amplitude of the perturbation, as discussed in a later section. As we shall see, however, we obtain an excellent qualitative agreement between the experiments and the simulations. This agreement indicates that the the basic pattern formation aspects of doublet structures

(such as the steady-state branch structure and the stability) do not seem to depend sensitively on the specific choice of model. This is most likely due to the fact that these aspects are dominated by the interaction between neighboring cell tips via diffusion of impurities in the liquid phase, which is present in both models.

The derivation of the equations of the phase-field model will be discussed in more detail elsewhere [28]. We write down here only what is necessary to reproduce the present computations. In a frame that is fixed with respect to the sample, i.e., where the isotherms move at velocity V_P along the z axis, the equations of the model take the form

$$\tau(\mathbf{n}) \partial_t \psi = (1 - \psi^2) \left[\psi + \alpha (\psi^2 - 1) \left(u + \frac{z - z_0 - V_P t}{l_T} \right) \right]$$
$$+ \vec{\nabla} \cdot [W(\mathbf{n})^2 \vec{\nabla} \psi] + \partial_x \left(|\vec{\nabla} \psi|^2 W(\mathbf{n}) \frac{\partial W(\mathbf{n})}{\partial \psi_x} \right)$$
$$+ \partial_z \left(|\vec{\nabla} \psi|^2 W(\mathbf{n}) \frac{\partial W(\mathbf{n})}{\partial \psi_z} \right), \quad (1)$$

$$\partial_t u = D \nabla^2 u + \frac{1}{2} \partial_t \psi, \quad (2)$$

where ψ is the phase field that varies between $+1$ in the solid and -1 in the liquid, u is a dimensionless measure of the chemical potential that varies slowly across the interface, α is the coupling constant between ψ and W, which is also proportional to the ratio $\sim W/d_0$, where d_0 is the chemical capillary length, z_0 is the reference position of the steady-state planar interface, and $l_T = m \Delta C/G$ is the thermal length, where m is the magnitude of the liquidus slope and G is the strength of the externally imposed temperature gradient.

In the appropriate thin-interface limit where the kinetics are made to vanish [1], the equations of the phase-field model reduce to those of the standard symmetric model defined in a moving frame by [30]

$$(\partial_t - V_P \partial_z) u = D \nabla^2 u, \quad (3)$$

$$u_{int} = -d_0(\mathbf{n}) \kappa - (z_{int} - z_0)/l_T, \quad (4)$$

$$V_n = D(\partial_{\mathbf{n}} u|_S - \partial_{\mathbf{n}} u|_L), \quad (5)$$

where

$$d_0(\mathbf{n}) = \frac{5\sqrt{2}}{8\alpha} [W(\mathbf{n}) + \partial_\theta^2 W(\mathbf{n})], \quad (6)$$

z_{int} is the position of the interface, κ is the local interface curvature, V_n is the normal interface velocity, and u becomes a composition variable that is continuous at the solid-liquid interface and satisfies the far field boundary condition $u(z = +\infty) = -1$. This variable is defined by $u = (C - C_L^0)/\Delta C$ in the liquid and $u = (C - C_S^0)/\Delta C$ in the solid, where C_L^0 and C_S^0 are the equilibrium concentrations in the liquid and solid phases at temperature T_0, respectively, and $\Delta C = C_L^0 - C_S^0$. We note that the identification of u, defined as a chemical potential in the phase-field model, and as a composition variable that is continuous at the interface in the sharp-interface limit is only possible because $(\partial \mu/\partial C)_{C = C_L^0} = (\partial \mu/\partial C)_{C = C_S^0}$

in the present model. For this reason, the mathematical structure of this model is nearly identical to that of a pure melt, which is why all the results of [1] carry over directly here. The only main difference is the introduction of a temperature gradient that does not modify the properties of the asymptotics [28].

The largest computations for the spatially extended arrays with 30–50 cells were carried out on lattices of dimension 2048×700. Smaller lattices with 1–2 cells were required to determine the steady-state branch structure and the stability limits. We used standard centered finite difference formulas to discretize the spatial derivatives and a simple Euler time-stepping scheme. Computational parameters were chosen as $D = 2$, $V_P = 0.1$, $l_T = 250$, $\Delta x = 0.8$, $\Delta t = 0.0727$, $\alpha = 3.4074$, and

$$W(\mathbf{n}) = W_0 a_s(\mathbf{n})$$

$$= W_0(1 - 3\epsilon)\left[1 + \frac{4\epsilon}{1 - 3\epsilon} \frac{(\partial_x \psi)^4 + (\partial_y \psi)^4}{|\vec{\nabla}\psi|^4}\right], \quad (7)$$

with $W_0 = 1$ and $\epsilon = 0.0129$, and

$$\tau(\mathbf{n}) = \tau_0(1 - 3\delta)\left[1 + \frac{4\delta}{1 - 3\delta} \frac{(\partial_x \psi)^4 + (\partial_y \psi)^4}{|\vec{\nabla}\psi|^4}\right], \quad (8)$$

with $\delta = 0.003\,45$ and $\tau_0 = 0.9965$. In the sharp-interface limit, these parameters correspond to choosing $d_0/l_T = 1.04 \times 10^{-3}$, $V_P/V_C = 5.04$, a 1% anisotropy in surface energy, and vanishing kinetics after correcting for the small anisotropy contribution of the discrete lattice as discussed in [1]. The role of crystalline anisotropy was studied by repeating some of the computations without anisotropy. The corresponding parameters that cancel out the grid anisotropy and hence yield zero effective anisotropy in both the surface energy and the interface kinetics are $\epsilon = 0.0029$ and $\delta = -0.018$.

B. Numerical results

1. Steady-state branches

We define here the wavelength λ of the cellular array as the distance between two subsequent grooves of *equal* depth. With this definition, this wavelength is equal to the width of the spatially repeating cellular subunit, i.e., one cell for singlets and two cells for doublets. Hence λ has a discontinuous jump (of a factor of 2) at the bifurcation point of the doublet branch from the singlet branch. In order to represent both branches on the same plot in a continuous fashion, we have found it useful to define the dimensionless wavelength, or Peclet number $\mathrm{Pe} = \lambda V_P/nD$, where $n = 1$ for singlets and $n = 2$ for doublets. This wavelength is the distance between subsequent grooves independent of their depth for both singlets and doublets, scaled by the diffusion length D/V_P.

Both singlet and doublet branches were constructed by carrying out a series of simulations in a box of width $\lambda/2$. Such a box fits one-half of a singlet cell from groove to tip or one asymmetrical doublet cell from the deep groove to the shallow groove. In addition, it suppresses oscillatory instabilities described below, which occur on twice this wave-
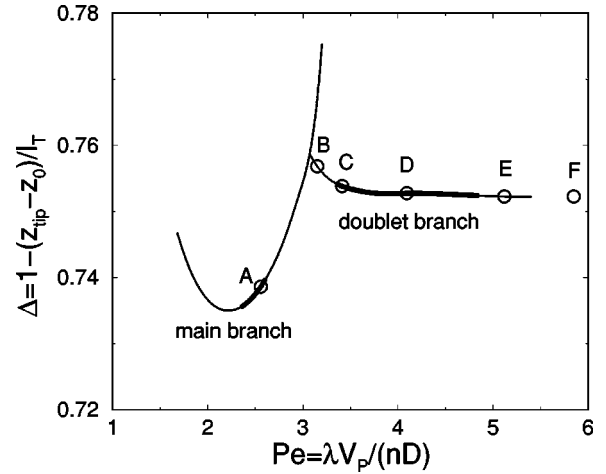

FIG. 8. Calculated singlet ($n = 1$) and doublet ($n = 2$) branches by the phase-field method where λ is the spacing between grooves of equal depth. The stable bands are indicated by a thick solid line. The symbols indicate the position along the branch structure of various simulated patterns.

length, and hence allows us to construct the whole steady-state branch. The results are shown in Fig. 8, where we plot the dimensionless tip undercooling $\Delta \equiv 1 - (z_{tip} - z_0)/l_T$, where z_{tip} is the position of the cell tip, as a function of Pe. The doublet branch bifurcates from the large spacing side of the singlet branch and shows little variation of the tip undercooling with wavelength. These results are in excellent agreement with our earlier boundary integral results [5].

2. Stability limits

Simulations were carried out to determine the stability limits of the singlet and doublet branches. From our previous boundary integral study of singlets [10], we know that the singlet array stability is limited at both small and large spacings by secondary instabilities that involve the motion of two cells. Accordingly, phase-field simulations were first carried out to check the stability limits of the singlet branch by using periodic boundary conditions in a computational box of width 2λ and by giving the two cells a small initial perturbation of wavelength 2λ. Stable and unstable cells were distinguished by examining whether perturbations damp out or grow in time. In agreement with our previous results [10], we found that the array stability is limited at small spacing by a nonoscillatory mode that gives rise to cell elimination leading to a doubling of the spacing. At large spacing, we found that stability is bounded by an oscillatory mode that gives rise to a vacillating-breathing (VB) motion of the cells, which has recently been characterized experimentally by Georgelin and Pocheau [11]. Also in agreement with our previous work [10], we found that the band of stable singlets becomes narrower with decreasing anisotropy strength and vanishes at a critical value, below which there are no stable singlets. For the 1% anisotropy reported in this study, there is a relatively narrow stable band that is indicated by the thick solid line portion of the singlet branch in Fig. 8.

Next we examined the stability of the doublet branch against perturbations of various wavelengths. We found that the stable band is limited at both small and large spacings by oscillatory modes that are illustrated in Fig. 9. Both modes
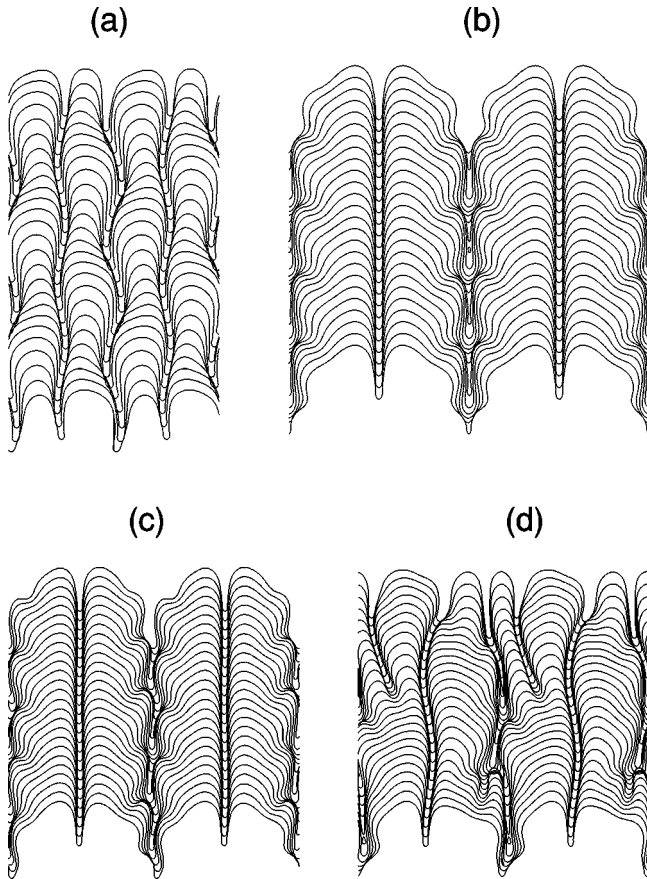
(a)   (b)

(c)   (d)

FIG. 9. Simulated oscillatory instabilities limiting the range of stable doublets at (a) small spacing (doublet vacillating breathing mode) and (b)–(d) large spacing (side-flapping mode). These simulations were carried out with periodic boundary conditions in a system with two asymmetrical cells corresponding to $\lambda V_P/D = 6.32$ (point B in Fig. 8) and $\lambda V_P/D = 10.8$ (point F in Fig. 8) in (a) and (b)–(d), respectively. For visualization purposes, all simulated patterns are repeated once laterally and the spacing between frames is about twice smaller in (a) than it would be on a one to one scale. A small amplitude noise (0.1 in units of lattice spacing) was added to the ψ field in the initial condition to trigger the instability in (a) and (b). In (c) and (d) we used an asymmetrical perturbation of the steady-state doublet profile $\psi_0(x,z)$ of the form $\psi(x,z) = \psi_0[x,z - A\Delta x \sin(2\pi x/\lambda)]$, with $x=0$ centered at the deep groove, and $A=2$ and $A=3$ in (c) and (d), respectively.

involve the motion of two cells or, equivalently, one wavelength of the doublet array according to our present definition of λ. On the low-spacing side, the mode is qualitatively similar to the VB mode that limits the stability of the singlet branch at large spacing. In particular, it involves a similar vacillating motion of the grooves and breathing motion of the cell shapes. This indicates that there is some degree of continuity of this instability as one switches from the singlet to the doublet branch with increasing spacing. Clearly, infinitesimally close to the bifurcation point of the doublet branch from the singlet branch, doublets must be subject to the same VB instability as singlets because their shape asymmetry vanishes at this point. This asymmetry, however, increases away from this point and is seen here to have a stabilizing effect. In particular, Fig. 9 shows that the vacillation amplitude of the shallower groove is smaller than that of the deeper groove. In this respect, the doublet VB mode is qualitatively different from the singlet VB mode, where grooves vacillate with the same amplitude.

On the high-spacing side, the mode produces an oscillatory flapping motion of the long sides of the asymmetrical cells and the central shallow groove remains quasistationary. We shall refer hereafter to this second oscillatory motion as the ''side-flapping'' (SF) mode. This motion is deterministically driven, in contrast to sidebranching, which is driven by noise. One important point concerning this instability should be emphasized. Although the fastest growing mode starting from a noisy perturbation of the steady-state doublet is symmetrical about the axis of the deep groove [Fig. 9(b)], asymmetrical modes [Fig. 9(c)] can also be obtained if a *finite* amplitude asymmetrical perturbation is applied initially. In this case, the deep groove sways from left to right as seen experimentally at large spacing in Fig. 5. Interestingly, the nonlinear character of this mode turns out to be very sensitive to the amplitude of this perturbation. Below a threshold amplitude, the asymmetrical flapping motion is sustained apparently indefinitely on the time scale of our simulations. In contrast, above this threshold, the bump generated at each oscillation eventually grows out into a new cell that becomes part of the array [Fig. 9(d)], as also observed experimentally in Fig. 5. This instability can therefore play an analogous role for doublets as ternary branching for dendritic arrays. We suspect that the asymmetrical SF mode is experimentally more common than the symmetrical one since small asymmetrical perturbations are generically present. The band of stable doublets, which is sandwiched between these two oscillatory instabilities, is shown by the thick solid line in Fig. 8. Note that this band is much wider than the band of stable singlets.

Finally, when we repeated the same stability study with zero anisotropy we found no stable doublets. This indicates that, as for the singlet branch, the width of the band of stable doublets decreases with decreasing anisotropy and vanishes at some small critical anisotropy. We did not determine this critical value and can only conclude that it lies somewhere between 0% and 1%. In addition, we cannot rule out the possibility that for other parameters (growth velocity, temperature gradient, etc.) doublets could be stable over some range of spacing without anisotropy.

3. Pattern selection in spatially extended systems and comparison with experiment

Our computationally efficient phase-field approach enables us to perform computations in spatially extended systems that can be compared to the experimental results of Sec. II B. Experimentally, a periodic perturbation cannot realistically be applied without tiny variations in phase and amplitude. Accordingly, to mimic such a perturbation in the simulations, we used as initial condition a steady-state planar interface moving at the pulling velocity V_P with a sinusoidal perturbation of amplitude A_p and wavelength λ_P, together with a small superimposed noise of amplitude A_n. Numerically, this translates into choosing at $t=0$
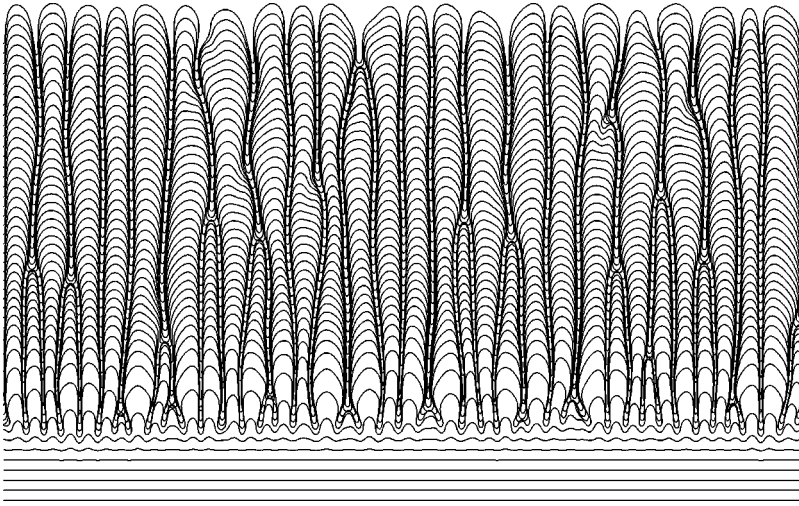
$$u(x,z) = u_{1D}(z), \qquad (9)$$

FIG. 10. Evolution of the interface starting from a planar interface with a small noise in the initial condition ($A_p = 0$ and $A_n = 0.01$). Here and in all subsequent figures the spacing between frames along the z axis is 1.3 times larger than it would be on a one to one scale.

$$\psi(x,z) = \psi_{1D}[z - A_p \Delta x \, \cos(2\pi x/\lambda_P) - A_n \Delta x \, \eta_i], \tag{10}$$

where η_i are independent random numbers chosen in the interval $[-1,1]$, i is an integer that defines the lateral position on the lattice, and $u_{1D}(z)$ and $\psi_{1D}(z)$ are the one-dimensional u and ψ profiles corresponding to an unperturbed steady-state planar interface. Values of the function $\psi_{1D}(z)$ were computed by interpolating through the known values, $\psi_{1D}(j\Delta x)$, on lattice points. To mimic the experimental situation where the instability is started from a planar interface we only use a small noise, which is equivalent to setting $A_p = 0$ in Eq. (10) above. We have not incorporated thermal noise in the present simulations because we have focused primarily on deterministic aspects of pattern selection by periodic perturbations. We expect that in cases where the selection is robust to the addition of a small noise in the initial condition, thermal noise should not have a strong influence. However, thermal noise could potentially affect selection runs that lead to only partially ordered arrays.

The simulation started with a noisy perturbation is shown in Fig. 10 and is to be compared to Fig. 4 in Sec. II B. As in the experiment, the interface undergoes continuous tip splitting and cell overgrowth. The interface shows signs of developing doublet structures, but it never reaches a steady state even after continuing the simulation four times longer than shown in Fig. 10. Different random initial conditions (i.e., different set of η_i) lead to the same qualitative picture. Therefore, in agreement with experiment, the simulations demonstrate that no stable doublet or singlet state can be reached dynamically from a planar interface for this range of velocity ($V_P/V_C = 5.04$) and surface tension anisotropy ($\epsilon = 1\%$).

The results of the simulations for the periodic perturbations are summarized in Table III. They confirm the expectation that an ordered array of singlets can be robustly selected from a periodic perturbation with a wavelength that falls within the stable band of singlets shown in Fig. 8. Moreover, they demonstrate that, as in the experiments described earlier, doublets can be selected if the wavelength is chosen within the stable band of doublets shown in Fig. 8. Hence, since doublets are stable over a broader range of wavelength than singlets, they can be selected over a broader range of λ_P.

The doublet selection runs show good overall qualitative agreement with experiment. After an initial transient, the interface settles into a stable periodic array of doublets and the final state has the same wavelength as the perturbation. The dynamical selection mechanism in the run of Fig. 11(d) is qualitatively similar to the experimentally observed mechanism in Fig. 2. In both sequences, the interface first develops a periodic array of very shallow cells with the same wavelength as the perturbation [see the fifth frame from the bottom of Fig. 11(d)]. Subsequently, these transient shallow cells tip split [see the sixth to eighth frames from the bottom of Fig. 11(d)] and their centers evolve into the deep grooves of the final doublets. Their initial grooves evolve into the shallower grooves of the final stable doublets. In contrast, a close examination of the frame sequence in Figs. 11(a) and 11(f) shows a qualitatively different transition. In this case, the grooves and tips of the initial perturbation end up forming the deep and shallow grooves of the final doublet array, respectively.

The simulated interface dynamics outside the range of stable doublets agrees qualitatively well with experiment. In agreement with Fig. 6, simulations (not shown here) demonstrate that fewer asymmetric doublets, i.e., with a smaller wavelength close to the singlet branch, are unstable. These doublets appear to be initially stable, but are eventually destroyed by the VB instability that leads to an overgrowth of some of the cells and a spatiotemporally chaotic final state. In turn, the simulation of Fig. 11(f) shows that more asymmetric doublets on the larger-wavelength side of the stable doublet band are unstable to the SF mode described in Fig. 9(b). Since the wavelength corresponding to this simulation is smaller (and hence closer to the stable band) than the one used in Fig. 9(b), the oscillations are of much smaller amplitude and visible only on the upper part of Fig. 11(f). A close examination of the cell shape in a continuation of this run reveals that there are sustained small-amplitude flapping oscillations. The experimentally observed instability at large doublet spacing (Fig. 5) is both of larger amplitude and asymmetrical. As noted earlier, it corresponds more directly to the SF instability shown in Figs. 9(c) and 9(d), which is produced by asymmetrical perturbations. Finally, as we further increase λ_P towards point F in Fig. 8, we find that the array stability is again destroyed, which leads to a spatiotemporally chaotic pattern illustrated in Fig. 11(h).

TABLE III. Simulated spatially extended interface patterns for periodic perturbations with V_P/V_C $=5.04$, $d_0/l_T=1.04\times10^{-3}$, and 1% anisotropy. The letter in parentheses in column 1 refers to the position of the perturbation wavelength on the steady-state branches of Fig. 8.

$\lambda V_p/D$	A_p	A_n	Final pattern	Figure
2.559 (A)	1	0	ordered array of singlets	not shown
2.559 (A)	1	0.001	ordered array of singlets	not shown
6.823 (C)	0.1	0.0001	ordered array of doublets	11(a)
6.823 (C)	0.1	0.001	partially ordered array of doublets	11(b)
6.823 (C)	1	0	partially ordered array of doublets	not shown
6.823 (C)	1	0.001	chaotic pattern	not shown
6.823 (C)	10	0.001	chaotic pattern	11(c)
8.188 (D)	0.1	0.001	chaotic pattern	not shown
8.188 (D)	1	0	ordered array of doublets	not shown
8.188 (D)	1	0.001	ordered array of doublets	11(d)
8.188 (D)	1	0.01	partially ordered array of doublets	11(e)
8.188 (D)	10	0.001	ordered array of doublets	not shown
10.235 (E)	1	0.001	ordered array of oscillatory doublets	11(f)
10.235 (E)	1	0.01	mixed array of doublets and triplets	11(g)
10.235 (E)	10	0.001	partially ordered array of triplets	not shown
11.697 (F)	1	0.001	chaotic pattern	11(h)

In addition, the simulations reveal that the dynamical selection of doublets depends on the amplitude (A_p) of the periodic perturbation as well as to the amplitude (A_n) of the noise, even if A_n is much smaller than A_p. Interestingly, the range of A_p that successfully leads to the selection of doublets, as opposed to a chaotic pattern, depends on the nature of the initial interface transient. For example, in Fig. 11(b), doublets are successfully selected for a small $A_p=0.1$ because tip splitting occurs during the initial transient as described above. If A_p is chosen 10 or 100 times larger with the same A_n, this splitting is prevented and a chaotic pattern is formed instead, as illustrated in Fig. 11(c). In contrast, for larger λ_P (see the runs corresponding to point D), $A_p=0.1$ does not lead to doublet selection, but for $A_p=1$ and $A_p=10$ doublets are robustly selected because the transient is different, as can be seen in Fig. 11(e).

The simulation results indicate that doublet selection by a purely sinusoidal periodic perturbation is sensitive to noise. This is to be expected because tiny initial irregularities become amplified during the initial transient. As a result, the sequence of cell elimination and splitting processes that leads to doublet selection may not occur synchronously along the interface. However, the results of Sec. II B show that ordered arrays of doublets can be obtained reproducibly in the presence of noise. This suggests that the presence of harmonics in the shape of the modulation (see Figs. 1 and 3), which is not included in the simulations, strongly enhances the evolution toward stable steady-state doublets. As shown in Sec. II B, the harmonic of the perturbation wavelength

closest to the natural initial instability wavelength grows fastest during the doublet evolution. This ensures that the wavelength of the mode that becomes dominant during doublet formation is a harmonic of the modulation wavelength and in phase with the modulation as long as the amplitude of noise is sufficiently smaller than the amplitude of the harmonic.

In order to test the conjecture that a harmonic of the modulation wavelength renders doublet selection more robust to noise, we performed an additional series of simulations by substituting $A_p\Delta x\cos(2\pi x/\lambda_P)$ in Eq. (10) with $A_p\Delta x\cos(2\pi x/\lambda_P)+A_{hp}\Delta x\cos(4\pi x/\lambda_P)$. The results are shown in Fig. 12. They demonstrate that, with a harmonic present ($A_{hp}/A_p=0.1$) and a small noise ($A_n/A_p=0.001$), an ordered array of doublets is selected that was not previously selected with a purely sinusoidal perturbation and the same noise level. Therefore, the selection is robust to the addition of a small noise. However, for a larger noise level (ten times smaller than the amplitude of the harmonic $A_n/A_{hp}=0.1$) only a partially ordered array is obtained. This array nevertheless still contains ordered regions of three or four doublets. This suggests that, in the experiments of Sec. II B, doublet selection is robust to a noise level about ten times smaller than the amplitude of the harmonic because the system only contains a few doublets. If the same experiments were repeated in a larger system, it is possible that only partially ordered arrays would be obtained for the same noise level. This remains an interesting issue to be explored.
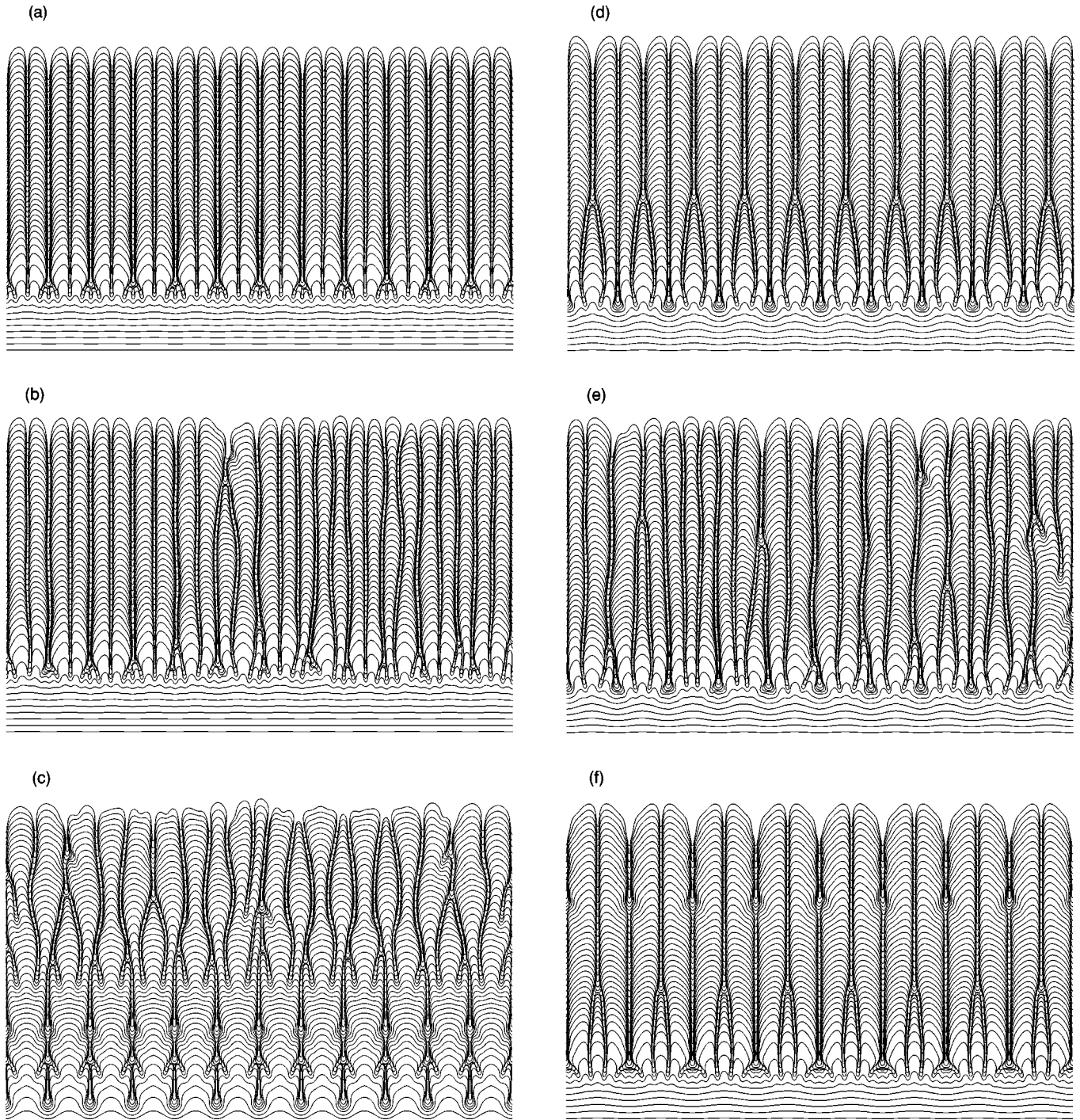
(a)

(d)

(b)

(e)

(c)

(f)

FIG. 11. Evolutions of the interface for various periodic perturbations of amplitude A_p, wavelength λ_P, and a small superimposed noise of amplitude A_n: (a) $\lambda_P V_P/D = 6.823$, $A_p = 0.1$, and $A_n = 0.0001$; (b) $\lambda_P V_P/D = 6.823$, $A_p = 0.1$, and $A_n = 0.001$; (c) $\lambda_P V_P/D = 6.823$, $A_p = 10$, and $A_n = 0.001$; (d) $\lambda_P V_P/D = 8.188$, $A_p = 1$, and $A_n = 0.001$; (e) $\lambda_P V_P/D = 8.188$, $A_p = 1$, and $A_n = 0.01$; (f) $\lambda_P V_P/D = 10.235$, $A_p = 1$, and $A_n = 0.001$; (g) $\lambda_P V_P/D = 10.235$, $A_p = 1$, and $A_n = 0.01$; and (h) $\lambda_P V_P/D = 11.697$, $A_p = 1$, and $A_n = 0.001$.

IV. DISCUSSION AND CONCLUSIONS

In this paper we have presented experimental and phase-field model simulation results on the formation of doublet structures with and without a periodic perturbation. Both experiments and simulations show that a brief periodic perturbation with a well defined wavelength, applied before the planar interface instability has set in, can result in an interface consisting of stable doublets. The perturbation brings the system into its steady doublet state rapidly and selects a uniform spacing if the noise superimposed on the periodic perturbation is sufficiently small. Experiments and simulations further indicate that the doublet pattern is stable for a range of doublet spacings and growth velocities. The experiments indicate that the range of spacings is largest in the region where some doublets appear transiently without a perturbation.

Outside the range of stable doublet spacings, different transient and stable patterns are observed. Figure 13 summa-
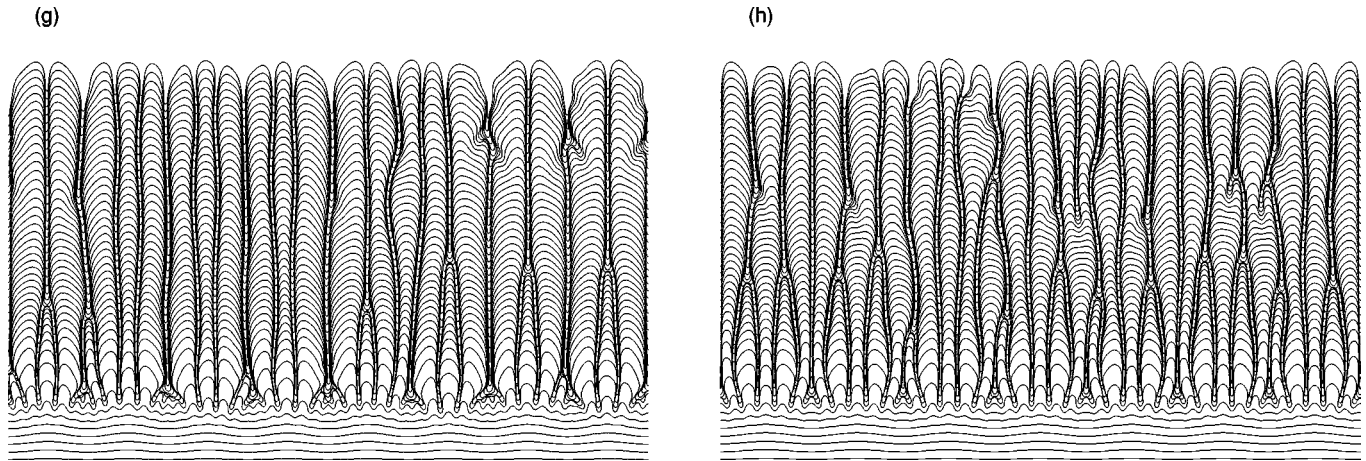
(g)

(h)

FIG. 11. (*Continued.*)

rizes the patterns observed as a function of the perturbation wavelength.

Transient doublets are observed in experiments and the simulations adjacent to the range of stable doublets. In the long-wavelength limit a breathing instability is observed (which eventually leads to the "birth" of new cells in some experiments and simulations). In the small-wavelength limit,
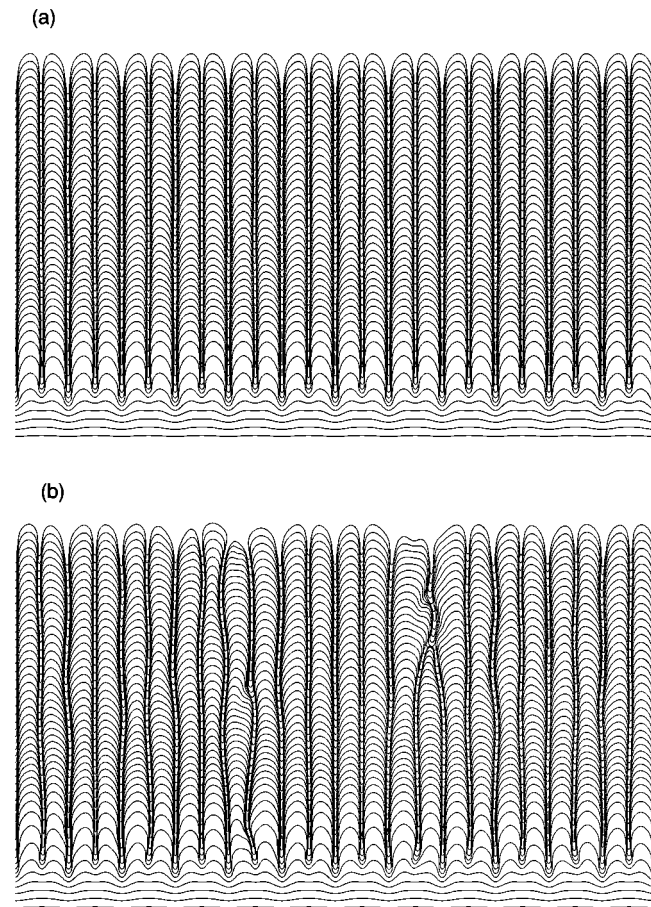
(a)

(b)

FIG. 12. Interface evolutions for an initial periodic perturbation of amplitude A_p with a superimposed harmonic of amplitude A_{hp} and a noise of amplitude A_n: (a) $A_p=1$, $A_{hp}=0.1$, and $A_n=0.001$; (b) $A_p=1$, $A_{hp}=0.1$, and $A_n=0.01$. The initial perturbation wavelength $\lambda_P V_P/D=6.823$ corresponds to point C in Fig. 8.

the same oscillatory vacillating-breathing instability that limits the stability of singlets at large wavelength [10,11] is observed. This instability eventually leads to the overgrowth of some cells in both the experiments and the simulations and to a chaotic pattern. The range of perturbation wavelengths where transient doublets are observed is narrow. For smaller wavelengths transient doublets are observed only briefly and the steady-state interface consists of an array of regular cells. For wavelengths far larger than the stable doublet range the interface displays spatiotemporal chaos from the start without transient doublets.

In the absence of a perturbation, the system never reaches stable uniform rows of doublets in experiment or simulations and displays only inclusions of transient doublets and other multiplet states. This indicates that the stable doublet state is not accessible in the noise initiated evolution from a planar interface, but can be accessed in experiments and simulations through a spatially periodic perturbation of the planar interface during the initial transient. The natural initial instability wavelength of the planar interface (observed in unperturbed experiments) still influences the dynamics of doublet formation, but the perturbation wavelength sets the steady-state doublet spacing. In addition, the presence of a harmonic of the perturbation wavelength both enhances, and renders more robust to noise, the selection of ordered arrays of doublets.
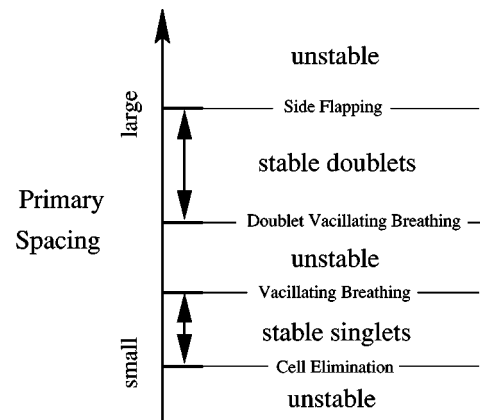

FIG. 13. Patterns observed in experiments and simulations as a function of the perturbation wavelength.

Triplets or higher-order multiplets, found in boundary integral calculations [5], were typically only transiently present in experiments and simulations. Therefore, these states are either dynamically unstable, have a small stability region, or cannot be triggered by sinusoidal modulations. In one isolated case, we did observe oscillatory triplets that appear to be stable [Fig. 11(g)]. However, it cannot be ruled out that this state is a long transient. The dynamics of decay of transient doublets, observed in experiments and simulations just outside the range of stable doublets, indicates that doublets are most unstable against a perturbation wavelength of the doublet spacing (twice the symmetric cell spacing).

In contrast to earlier phase field models, this form of the phase-field model gives quantitatively accurate results (as verified in [1,28]). Unfortunately, at this point they cannot be compared quantitatively to the experimental results since the simulations employ the symmetric model of binary alloy solidification with a constant concentration jump at the interface while the experimental system is best described by the one-sided model with a segregation coefficient different than unity. In addition, in the simulations the ratio of capillary length to thermal length (d_0/l_T) is three orders of magnitude larger than in the present experiments. Despite these differences, for all steady-state patterns and dynamical instabilities, the phase-field simulations and the experiments show excellent agreement. This indicates that the ratio between V_P and V_C and the surface tension anisotropy, which are comparable in experiments and simulations, are important parameters for pattern selection and pattern stability.

The pattern selection method presented in this paper, based on applying a brief spatially periodic perturbation to the solid-liquid interface of a solidifying sample, alters the natural selection process, provides a direct experimental way of accessing patterns not selected during the evolution from an unperturbed planar interface, and permits exploring the stability of cellular patterns over a large range of spacings.

ACKNOWLEDGMENTS

[1] A. Karma and W.-J. Rappel, Phys. Rev. E **53**, R3017 (1996); Phys. Rev. Lett. **77**, 4050 (1996); Phys. Rev. E **57**, 4323 (1998).

[2] W. Kurz and R. Trivedi, Acta Metall. Mater. **38**, 1 (1990).

[3] W. W. Mullins and R. F. Sekerka, J. Appl. Phys. **35**, 444 (1964).

[4] H. Jamgotchian, R. Trivedi, and B. Billia, Phys. Rev. E **47**, 4313 (1993).

[5] P. Kopczyński, A. Karma, and W.-J. Rappel, Phys. Rev. E **55**, 1282 (1997).

[6] W.-J. Rappel, Phys. Rev. E **48**, 4118 (1993).

[7] A. Karma and W.-J. Rappel, Phys. Rev. Lett. **75**, 2444 (1995).

[8] S. Akamatsu, G. Faivre, and T. Ihle, Phys. Rev. E **51**, 4751 (1995).

[9] T. Ihle and H. Müller-Krumbhaar, Phys. Rev. Lett. **70**, 3083 (1993); Phys. Rev. E **49**, 2972 (1994).

[10] P. Kopczyński, A. Karma, and W.-J. Rappel, Phys. Rev. Lett. **77**, 3387 (1996).

[11] M. Georgelin and A. Pocheau, Phys. Rev. Lett. **77**, 2698 (1997).

[12] S. A. Curtis and J. V. Maher, Phys. Rev. Lett. **63**, 2729 (1989).

[13] M. A. Chopra, M. E. Glicksman, and N. B. Singh, Metall. Trans. A **19**, 3087 (1988).

[14] K. Soomboonsuk, J. T. Mason, and R. Trivedi, Metall. Trans. A **15**, 967 (1984).

[15] R. Trivedi and K. Soomboonsuk, Mater. Sci. Eng. **65**, 65 (1984).

[16] L. H. Ungar and R. A. Brown, Phys. Rev. B **29**, 1367 (1984).

[17] W. Losert, B. Q. Shi, and H. Z. Cummins, Proc. Natl. Acad. Sci. USA **95**, 431 (1998).

[18] M. E. Glicksman, R. J. Schaefer, and J. D. Ayers, Metall. Trans. A **7**, 1749 (1976).

[19] M. Muschol, D. Liu, and H. Z. Cummins, Phys. Rev. A **46**, 1038 (1992).

[20] Reference sheet Sigma Chemical Company.

[21] E. R. Rubinstein, S. H. Tirmizi, and M. E. Glicksman, J. Cryst. Growth **106**, 89 (1990).

[22] L. Williams *et al.*, Phys. Rev. E **48**, 489 (1993).

[23] H. Chou and H. Z. Cummins, Phys. Rev. Lett. **61**, 173 (1988).

[24] J. A. Warren and J. S. Langer, Phys. Rev. E **47**, 2702 (1993).

[25] C. Misbah, H. Müller-Krumbhaar, and Y. Saito, J. Cryst. Growth **99**, 156 (1990).

[26] J. S. Langer, *Directions in Condensed Matter* (World Scientific, Singapore, 1986), p. 164.

[27] A. Karma and W.-J. Rappel, Phys. Rev. Lett. **77**, 4050 (1996).

[28] P. Kopczyński, A. Karma and W.-J. Rappel (unpublished).

[29] J. S. Langer and L. A. Turski, Acta Metall. **25**, 1113 (1977).

[30] J. S. Langer, Acta Metall. **25**, 1121 (1977).